

Semester Thesis

**Acceleration Cage for
Atomic Electron Detection
in Cold Muonium
Antimatter Gravity
Experiment**

Autumn Term 2020

Contents

Abstract	iii
1 Introduction	1
1.1 Theoretical Background	1
1.1.1 The Standard Model	1
1.1.2 Beyond the Standard Model	2
1.2 PSI's Muonium Antimatter Gravity Experiment	3
1.2.1 Interferometry	4
1.2.2 Cold Beam	4
1.2.3 Detection	4
1.3 Proof-of-Principle Experiment	5
1.3.1 Closed-Cycle ^3He Cryostat	5
1.3.2 Target Cavity	8
2 Methods	11
2.1 Modifications of the ^3He Cryostat	11
2.2 Acceleration Grid Setup	12
2.2.1 COMSOL Simulation	12
2.2.2 G4beamline Simulation	12
2.2.3 Conductive PLA Tests	14
3 Results and Discussion	15
3.1 Modifications of the ^3He Cryostat	15
3.2 Acceleration Grid Setup	16
3.2.1 COMSOL Simulation	16
3.2.2 G4beamline Simulation	22
3.2.3 Conductive PLA Tests	24
4 Conclusion	27
Acknowledgements	29
Bibliography	31
Declaration of Originality	33

Abstract

In this semester thesis, progress towards PSI's novel muonium antimatter gravity experiment is presented. The experiment consists of three main stages that are developed simultaneously: (1) the creation of a high quality cold muonium beam, (2) interferometry involving muonium atoms and (3) the detection of muonium decays. Developments in stage (1) involved the modification of the closed-cycle ^3He cryostat used for this experiment to reach the desired operating temperatures. By improving the pre-cooling, the temperature in the target was reduced from 0.5 K to 0.42 K. Possible further modifications that could bring the temperature down to the required 0.3 K are discussed.

For stage (3), a coincidence technique featuring the detection of the atomic electrons accelerated onto a scintillator read out by a SiPM is being developed. The cage accelerating atomic electrons to roughly 10 keV should not interfere with the muonium production and reject secondary electrons from the surrounding material. Here, the design for a cage setup meeting these requirements is presented and analyzed both in *COMSOL* and *G4beamline* simulations. It has an overall atomic electron detection probability of 85.2 %, rejects all electrons entering from the side and the top and features field strengths below 80 V cm^{-1} at the bottom. In a feasibility study, the possibility of fabricating the acceleration cage using 3D-printing with conductive PLA was analyzed. While the room temperature tests were promising, we could not conduct cryogenic tests.

Chapter 1

Introduction

1.1 Theoretical Background

1.1.1 The Standard Model

According to our current knowledge, all physical processes that take place in the universe are governed by four fundamental forces. Three of them – the electromagnetic, the strong and the weak force – are described by the Standard Model (SM) of particle physics. The elementary fermions of the SM and the gauge bosons that mediate the forces are listed in Figure 1.1.

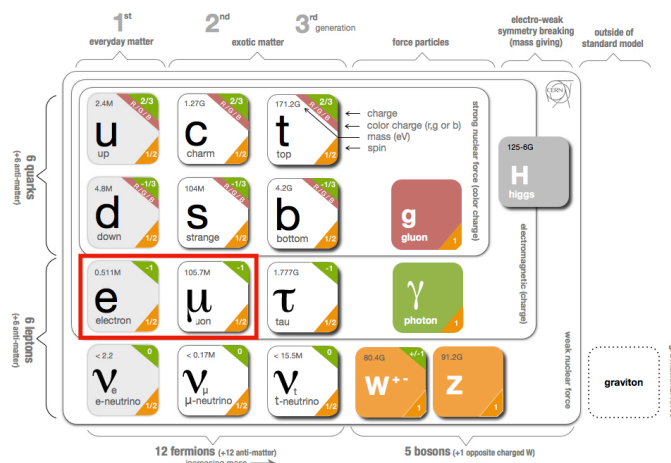


Figure 1.1: Overview over the particles in the Standard Model. The three fundamental forces are mediated by four gauge bosons. The fermions are separated into two sectors (quarks, leptons) and three generations (1st, 2nd, 3rd).

(Source: <http://united-states.cern/physics/standard-model-and-beyond>)

The two fermions indicated in red – the electron (e^-) and the muon (μ^-) – are the main actors of this study. To our current knowledge, both are point-like elementary particles, as they do not evince finite-size effects up to the length scales attainable by LHC. They interact via the electromagnetic and the weak force, but not via the strong force, hence they are attributed to the so-called lepton sector. While the electron is part of the 1st generation – the particles that make up everyday matter –, the muon belongs to the 2nd generation and is much less abundant.

Each fundamental fermion has a corresponding antiparticle. Antifermions have charges inverse to that of fermions, otherwise they share the same quantum numbers and (inertial) masses. The antifermions of the electron and the muon are called positron (e^+) and antimuon (μ^+), respectively. The antimuon can form a bound state with an electron, the resulting exotic atom is called muonium (Mu). Mu atoms are very similar to hydrogen, with the only difference that the composite proton in the center was replaced by the point-like antimuon.

The predictions of the SM have been tested in a multitude of experiments and verified to astounding precisions [1, 2].

1.1.2 Beyond the Standard Model

General Relativity

The fourth fundamental force, gravity, is not included in the Standard Model (as shown in Figure 1.1). It is a lot weaker than the other three fundamental forces. The most comprehensive mathematical description of gravity we have to date is Albert Einstein's theory of General Relativity. It is based on the weak equivalence principle, which states that the inertial mass (the resistance to accelerations) of an object is equal to its gravitational mass (the strength with which it couples to the gravitational field). This implies that all objects should fall at the same rate in a gravitational field.

Both the predictions of General Relativity as well as the equivalence principle stood the tests of many experiments [3–5]. The most stringent test of the equivalence principle, performed by the MICROSCOPE collaboration, yielded

$$\frac{m_{1g}}{m_{1i}} - \frac{m_{2g}}{m_{2i}} < 1.3 \times 10^{-14} \quad (1.1)$$

for m_1, m_2 consisting of two different metal alloys [6]. It can therefore be concluded that the weak equivalence principle has been tested thoroughly for normal matter.

Tests of the Weak Equivalence Principle in an Exotic Sector

For antimatter, however, experimental data is a lot more scarce. While the weak equivalence principle is generally believed to hold for antimatter as well, there could be extra interactions that break it. The only direct measurement of antimatter gravity to date yielded

$$-65 < \frac{\bar{m}_g}{m_g} < 110 \quad (1.2)$$

for hydrogen [7, 8], \bar{m}_g being the gravitational mass of antihydrogen. More stringent limitations based on indirect measurements (e.g. polarization effects or the anti-quark content of nucleons) exist [9], but these can only selectively rule out types of extra interactions. Via a more accurate direct measurement of gravitational interactions involving antimatter, one can probe for interactions breaking the weak equivalence principle in a general manner. Such a measurement therefore constitutes an important probe for beyond the Standard Model (BSM) physics [8]. In addition, it is a test of General Relativity in new territories and may provide new insights that help in unifying General Relativity with the Standard Model.

For these reasons, several experiments seeking to measure the acceleration of antimatter in Earth's gravitational field have been proposed or are already ongoing. The experiments ALPHA [10], AEGIS [11] and GBAR [12] at CERN based on antihydrogen (antiproton with an electron) are being pursued, experiments based on positronium (exotic atom consisting of a positron and an electron) have been discussed [13]. The novel muonium antimatter gravity experiment at PSI pursues a different path, working towards a direct antimatter gravity measurement with muonium [8].

Testing gravitational interactions involving antimatter with muonium is complementary to experiments with antihydrogen. Unlike the composite antiproton in antihydrogen, where the valence antiquarks contribute to only a few percent of the rest mass, the antimuon is an elementary antiparticle [8]. In addition, measuring the fall of muonium atoms in Earth's gravitational field would constitute the first gravity measurement involving second- or third-generation particles [8]. Also from this perspective PSI's muonium antimatter gravity experiment makes an important contribution to probing for beyond Standard Model physics in the exotic sector.

1.2 PSI's Muonium Antimatter Gravity Experiment

The muonium antimatter gravity experiment at PSI seeks to measure the gravitational acceleration of muonium atoms in Earth's gravitational field. It consists of three main stages that are being developed simultaneously:

- (1) the creation of a high quality cold muonium beam,
- (2) interferometry involving muonium atoms and
- (3) the detection of muonium decays.

A schematic drawing of the experimental setup is given in Figure 1.2. In the following, the three main stages will be discussed.

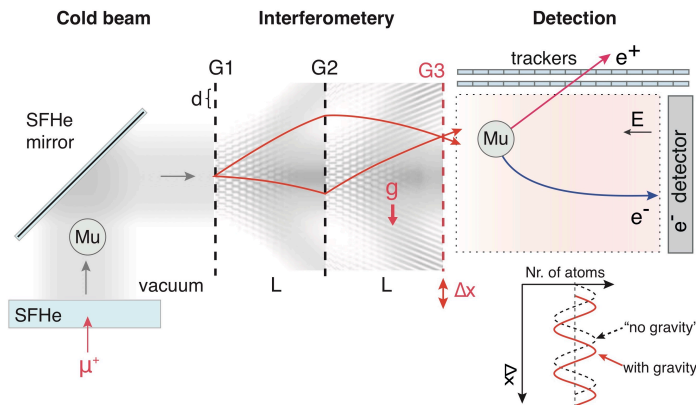


Figure 1.2: Schematic drawing of the MAGE experimental setup. It consists of three main stages: (1) the beam creation on the left, (2) the interferometer in the middle and (3) the detection of muonium decays on the right.

1.2.1 Interferometry

At the heart of the experimental setup lies a three-grating interferometer, shown in the middle of Figure [1.2](#). Diffraction on the first two gratings results in an interference pattern at the position of the third grating. Since the paths of massive particles are bent in Earth's gravitational field, also the the interference pattern is slightly shifted for massive particles compared to massless ones. The phase shift of the interference pattern therefore contains information about the gravitational acceleration of the beam particles. The phase shift is determined by scanning the third diffraction grating with a piezoelectric element, moving the grating up and down vertically. The spatial variation in beam intensity after the interferometer is thereby translated into a phase variation.

1.2.2 Cold Beam

In order to achieve the required interferometer stability, the incoming muonium beam (shown on the left of Figure [1.2](#)) must have a small transverse momentum and a narrow overall momentum distribution. In addition, a slow beam velocity (on the order of 1'000 m/s) is desirable. Conventional Mu converters (like aerogel or mesoporous SiO₂) provide thermal beams with wide angular and momentum distributions. In this experiment the development of a novel superfluid helium (SFHe) Mu converter is proposed that would provide a high quality beam amenable to interferometry. The incoming μ^+ beam is stopped in a thin ($\sim 100 \mu\text{m}$) layer of SFHe, which is cooled to 0.3 K. In the SFHe layer, the μ^+ neutralizes by combining with an ionization electron. The movement of the newly formed muonium atom is then governed by diffusion. If by coincidence the atom reaches the SFHe surface (the likelihood of which is increased by having muonium form close to the surface), it is ejected vertically from the SFHe with a uniform energy of 23.3 meV. This is due to an inherent property of SFHe: the muonium atoms constitute impurities in the SFHe layer, the overlap of the muonium and helium wavefunctions cause a raise of the muonium atom chemical potential. This raise was calculated to amount to 270 K, corresponding to the above-stated 23.3 meV. The transverse momentum of the muonium atom will not change upon being ejected, it will therefore amount to the Maxwell-Boltzmann average. The latter is sufficiently small for 0.3 K [\[14\]](#).

1.2.3 Detection

As described above, scanning the last grating of the interferometer with a piezoelectric actuator translates the spatial variations in muonium beam intensity to a phase variation. Subsequently, the intensity of the muonium beam needs to be measured as a function of the displacement of the third grating. This is done by recording all muonium decays that take place in the region after the interferometer, given a certain grating position. Muonium has a lifetime of 2.2 μs and decays via the weak decay of the μ^+ :

$$\text{Mu} \rightarrow e^+ + e^- + \bar{\nu}_\mu + \nu_e. \quad (1.3)$$

In order to distinguish a muonium decay from a μ^+ decay, both the atomic electron and the positron need to be detected. The positron has enough energy to create scintillation light by ionization in the surrounding detectors. The atomic electrons, on the other hand, are released from their bounded state having low kinetic energy. To be detected, they need to be collected and accelerated towards a scintillator, which can then be read out using silicon photomultipliers (SiPMs).

1.3 Proof-of-Principle Experiment

In a proof-of-principle experiment, the muonium production (stage (1) of the experiment) and the acceleration cage required to collect and detect the atomic electrons resulting from muonium decays (stage (3) of the experiment) must be tested. The experimental setup of this experiment is given in Figure 1.3. It involves a ^3He evaporation cryostat (displayed on the left in Figure 1.3) that should cool the cylindrical target chamber with a radius of 20 mm and a height of 40 mm (on the right) to 0.3 K. Cooling the setup to such low temperatures is necessary to have a low enough ^4He vapor pressure in the cavity not to interfere with the Mu beam. The μ^+ beam is entering the cavity from the bottom through a 100 μm thin titanium foil and is stopped in the SFHe layer, where the μ^+ neutralize and muonium forms. The Mu atoms are then ejected upwards from the SFHe layer. After having travelled a few cm in the cavity, the Mu atoms decay, thereby releasing a fast positron and a slow atomic electron. The atomic electrons have to be accelerated towards the scintillator placed at the top of the cavity (see Figure 1.3 on the right).

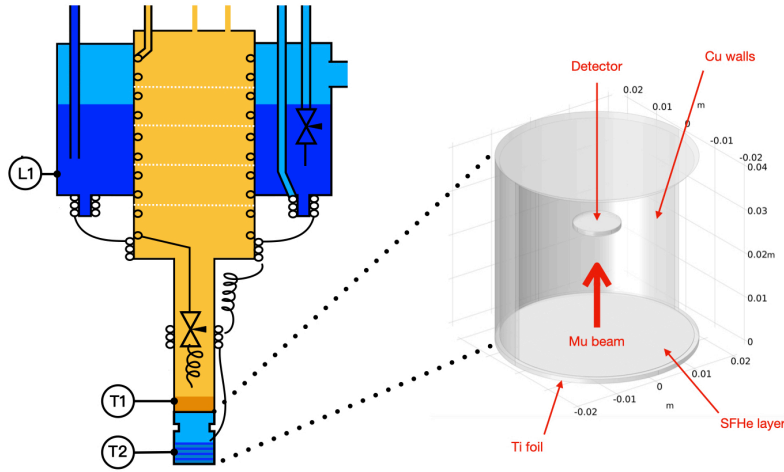


Figure 1.3: Schematic representation of the setup for the proof-of-principle experiment. The main part of the closed-cycle ^3He evaporation cryostat is shown on the left, the cylindrical target chamber is displayed on the right. μ^+ particles enter from the bottom, are stopped in the SFHe layer and form Mu atoms. These are ejected from the layer, travel a few cm in the cavity and decay. The daughter atomic electrons need to be collected and accelerated onto a scintillator using an acceleration cage.

1.3.1 Closed-Cycle ^3He Cryostat

An overview over the entire cryogenic setup is given in Figure 1.4. It features two main cycles: the open ^4He cycle displayed in blue and the closed ^3He cycle displayed in orange. A ^4He bath of $\sim 2.5\text{ K}$ (blue, cooled by a lambda-point refrigerator) is used to pre-cool the ^3He gas (orange), and liquefy it before it reaches the Joule-Thomson valve. The pressure of the liquid ^3He then suddenly drops as the liquid exits from the capillary, and enters a chamber (orange) evacuated by three pumping stages. Evaporative cooling is used in both cycles. It is based on the principle that heat is extracted from a system when a liquid transitions to the gaseous phase.

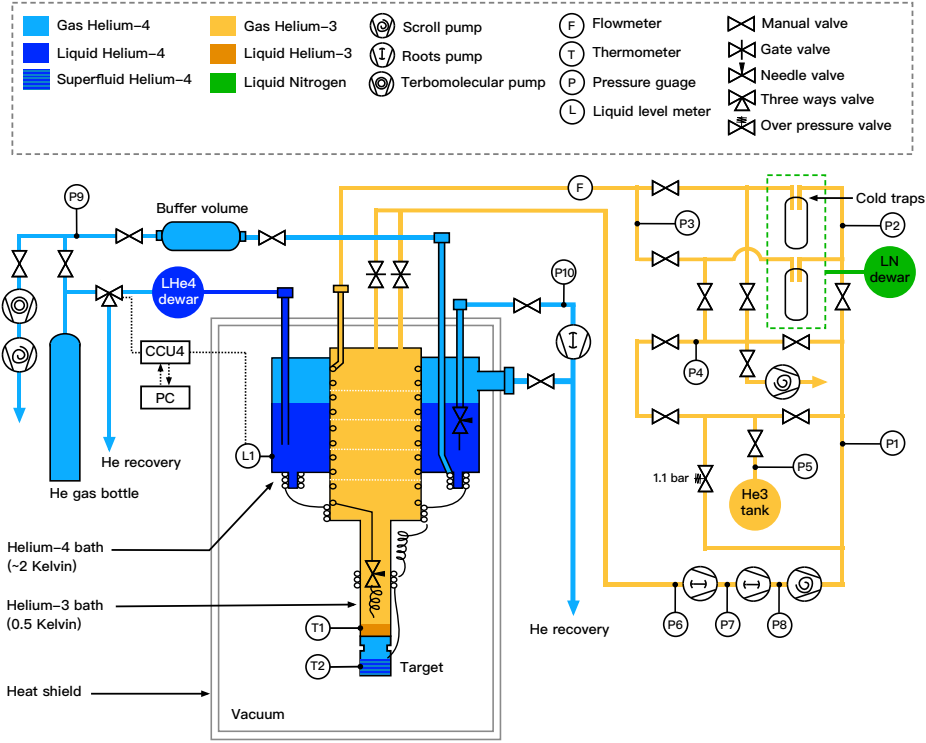


Figure 1.4: Schematic representation of the cryogenic setup. The blue parts represent the ^4He lines used to pre-cool the cryostat and to create the SFHe layer inside the target cavity. The orange parts represent the fully closed ^3He cycle of the evaporation cryostat.

Evaporative ^4He and ^3He Cooling

At atmospheric pressure, ^3He and ^4He boil at 3.2 K and 4.2 K, respectively (see Figure 1.5). The fact that both boiling points are very low, with the one for ^3He being slightly lower than the one for ^4He , can be explained by the quantum mechanical zero-point energy [15]. It is the kinetic energy resulting from the uncertainty in the momentum of the ground state and hence given by

$$E_0 = \frac{h^2}{8ma^2},$$

where $a = \left(\frac{V_m}{N_0}\right)^{1/3}$ is the radius of the sphere to which the atoms are confined and N_0 is Avogadro's number. The zero-point energy plays an important role in both helium isotopes, since their masses are small and van der Waals forces are weak due to the filled s-shell of helium [15]. It leads to the low boiling points in both isotopes, with the one for ^3He being slightly lower due to the lower mass. This is why helium belongs to the so-called quantum liquids and constitutes an ideal working liquid for cryostats.

At atmospheric pressures, ^3He boils at temperatures above 3.2 K, thus reducing the system's temperature by extracting heat of evaporation. At the boiling point, the liquid phase enters an equilibrium with the gaseous phase, the boiling reduces to the rate needed to compensate the incoming external heat flux. Therefore, 3.2 K is the lowest temperature that can be reached at this pressure.

By pumping on the gaseous phase, however, the vapour pressure can be reduced, thus shifting the equilibrium. The resulting boiling temperatures will follow the vapour pressure curves displayed in Figure 1.5. They have a $e^{-L/RT}$ -dependence (L being the latent heat of evaporation and R the gas constant), which means that also the cooling power at a fixed pumping rate will decrease with lower temperatures as $e^{-L/RT}$. This results in the lower temperature limits attainable via evaporative cooling of around 1.3 K and 0.3 K for ^4He and ^3He , respectively [15].

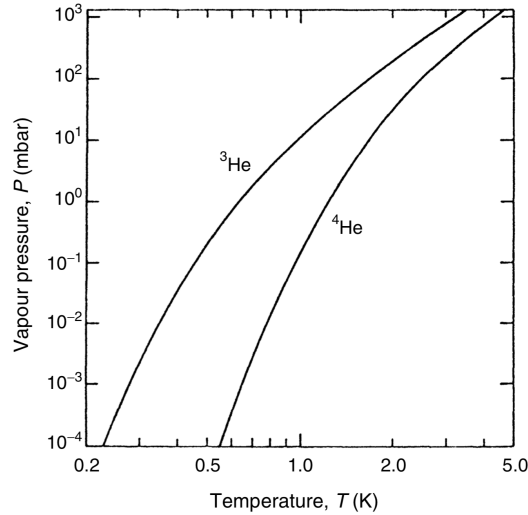


Figure 1.5: Vapor pressure curves of ^3He and ^4He . At atmospheric pressure, ^3He and ^4He boil at 3.2 K and 4.2 K, respectively. For lower pressures, the curve shows a $e^{-L/RT}$ -dependence. By pumping on the gaseous phase, the equilibrium can be shifted along the curve towards lower temperatures.

(Source: [15])

Evaporative cooling is used both for the ^3He and the ^4He cycle in the cryogenic setup. The roots and scroll pumps used to lower the helium vapor pressure are shown in Figure 1.4. While the ^3He cycle needs to be completely closed due to the high price of ^3He (hence the more sophisticated gas system shown in orange that is used to reliably control all stages of the cryostat), the extracted ^4He vapor can simply be discarded to the He recovery line.

Liquefaction and pre-cooling

Pre-cooling plays a crucial role in every cryogenic setup. Since the cooling power of a cryostat decreases with temperature (in the case of evaporative cooling it follows the $e^{-L/RT}$ -dependence of the vapor pressure curve [15]), pre-cooling stages at higher temperature are needed to compensate the external heat fluxes and to minimize the amount of (expensive) working liquids needed to reach the final temperature.

In our cryogenic setup, this is achieved via a ^4He stage that operates at roughly 2 K. The ^3He vapor coming back from the closed gas system is liquefied by the pre-cooling stage. From there, it passes through a needle valve that is used to control the ^3He flow and enters a small spiral tube (shown in Figure 1.4). In this tube, the entering helium is pre-cooled by the ^3He vapor that is pumped away from the ^3He bath. Having reached the end of the spiral tube, the ^3He gas expands against the external pressure, its temperature thereby being reduced further via the Joule-Thomson effect. The liquid ^3He that now enters the main bath should have a temperature that does not deviate significantly from the bath temperature.

1.3.2 Target Cavity

Acceleration Cage

In the following, the setup in the target cavity, shown on the right in Figure [1.3](#), will be discussed, in particular the cage needed to accelerate the atomic electrons. It has to meet several requirements. First and foremost, it needs to collect a high percentage of the electrons resulting from Mu decays and accelerate them to ~ 10 keV, so that they produce a signal in the scintillator at the top. Additionally, the electric fields of the acceleration cage should not interfere with the muonium formation taking place in the SFHe layer at the bottom. It was found in a previous test experiment that the external electric field should not exceed 100 V cm^{-1} in the layer. Finally, the acceleration cage should reject all secondary electrons freed by charged particles hitting the metal walls of the cavity, minimizing the detection of random coincidences.

Conductive PLA

In order to have a convenient and precise method to fabricate the acceleration cage, as well as to have few secondary electrons released by charged particles hitting the wires of the cage, 3D-printing using conductive PLA should be considered. The company ProtoPasta Inc. has released a novel conductive PLA only a few years ago. According to their website, it is a compound of Natureworks 4043D PLA, a dispersant and conducting carbon black [\[16\]](#). The latter are concentrically arranged continuous layers of hexagonally arranged carbon atoms to primary particles containing small graphitic or turbostratic domains. They are added as polymer fillers and build conducting networks by forming aggregates and agglomerates [\[17\]](#). A TEM image of agglomerated carbon black aggregates is given in Figure [1.6](#).

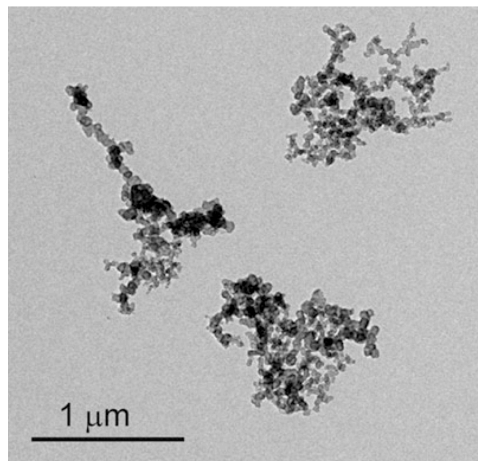


Figure 1.6: Aggregates of carbon black primary particles under the TEM. They are added to the PLA as polymer fillers and form conducting networks.

(Source: [\[17\]](#))

In a literature research, only one paper analyzing the conductivity of carbon black networks in polymers at different temperatures was found [\[18\]](#). Its results are displayed in Figure [1.7](#). $E_x N_y P_z$ indicates the composition of the polymer, the x in E_x being the proportion of Ethylene-vinyl acetate, the y in N_y the proportion of Nitrile rubber and the z in P_z the parts of Printex grade carbon black added as filler.

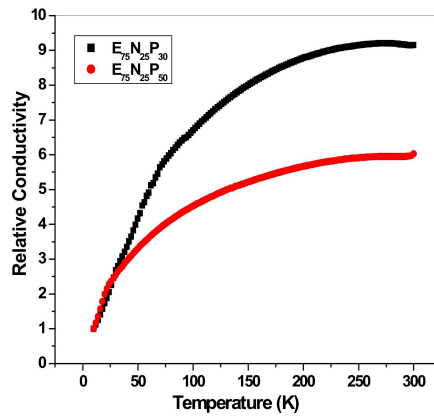


Figure 1.7: Conductivity of carbon black networks in a polymer at different temperatures. The conductivity seems to decrease at low temperatures, but the exact temperature dependence at cryogenic temperatures is not shown here.

(Source: [18])

The conductivity of the carbon black networks seems to decrease significantly at cold temperatures. But the exact temperature dependence at cryogenic temperatures is not shown here and the plot indicates that the conductivity is dependent on the polymer composition. Therefore, the exact temperature dependence of conductive PLA at cryogenic temperatures is still worthwhile to be analyzed.

Chapter 2

Methods

This chapter gives an overview over the methods that were used. First, the modifications of the closed-cycle ^3He cryostat that were implemented to lower its operating temperature (stage (1) of the experiment) are discussed. Then the software used to simulate the acceleration grid for the atomic electrons, as well as the 3D-printed conductive PLA samples that were used to analyze the conductivity of carbon black networks at room temperature (stage (3) of the experiment) are presented.

2.1 Modifications of the ^3He Cryostat

In a previous test experiment, the ^3He cryostat reached an operating temperature of 0.5 K, above the required 0.3 K. A probable cause for that is insufficient pre-cooling. The spiral tube below the needle valve in the ^3He cycle (see Figure 1.4) was not long enough to reach close to the ^3He bath. By elongating the spiral tube, the entering ^3He liquid spends more time being pre-cooled by the ^3He gas that is pumped away from the ^3He bath. In this way, pre-cooling is increased. The new spiral tube is shown on Figure 2.1

The cryogenic resistance temperature sensor, shown on the bottom left of Figure 2.1, was fixed to the cryostat insert using kapton tape and floss (waxed, without mint taste). In order to stabilize the elongated spiral tube to ensure that it does not get stuck while pushing in the ^3He insert, we fixed it with a plastic rod that we placed along the symmetry axis of the spiral tube.



Figure 2.1: Pictures of the cryostat insert. The spiral tube was elongated, so that the entering ^3He liquid spends more time being pre-cooled by the ^3He vapor.

2.2 Acceleration Grid Setup

2.2.1 COMSOL Simulation

The *Electrostatics* package of the finite elements solver and multiphysics simulation software *COMSOL* [19] was used to simulate the electric field of the acceleration grid. The electric fields were rendered in 3D using the *Stationary* solver. A screenshot of the software is given in Figure 2.2.

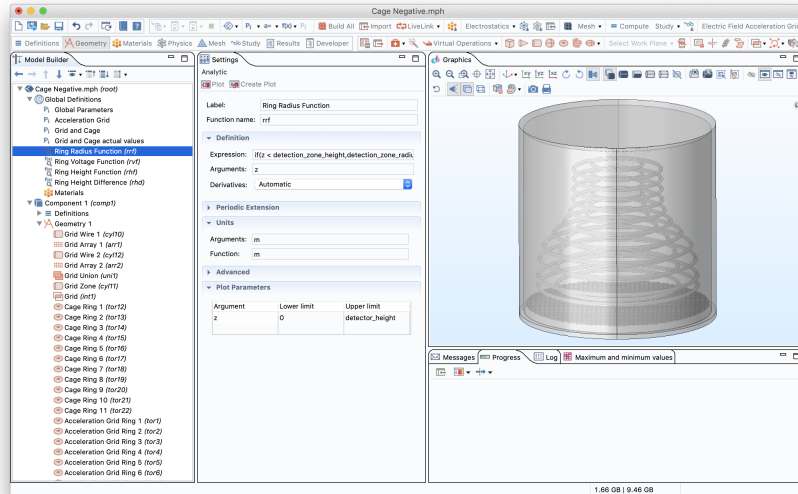


Figure 2.2: Screenshot of the *COMSOL* simulation. The fields of the acceleration grid were modelled in 3D using the *Electrostatics* package.

The radii and voltages of the cage rings were modeled adaptively with functions (the settings for the ring radius function are displayed in Figure 2.2). This allows for a convenient optimization of these parameters. The analytic expressions of the optimized functions are given in Section 3.2.1.

All cavity walls are put on ground, to set the boundary conditions for the *Stationary* solver rendering the electric field. The cage rings are put on the voltage defined by the ring voltage function at the respective height. *COMSOL's Physics Controlled-Mesh size Fine* was used to mesh the geometry. It automatically varies the mesh size depending on the complexity of the rendered geometry.

2.2.2 G4beamline Simulation

In principle, *COMSOL's Charged Particle Tracing* could be used to model the electron trajectories under the influence of the simulated fields. However, the simulations are rather time-consuming and *COMSOL* does not allow for more complicated beams to be simulated. Therefore, the simulations of the atomic electron trajectories were performed in the *G4beamline* environment. The rendered field values were exported from *COMSOL* to a .txt file and then imported in a *G4beamline* simulation using the *fieldmap* command. A mesh size of 1 mm was chosen for the field map, as shown in Figure 2.3.

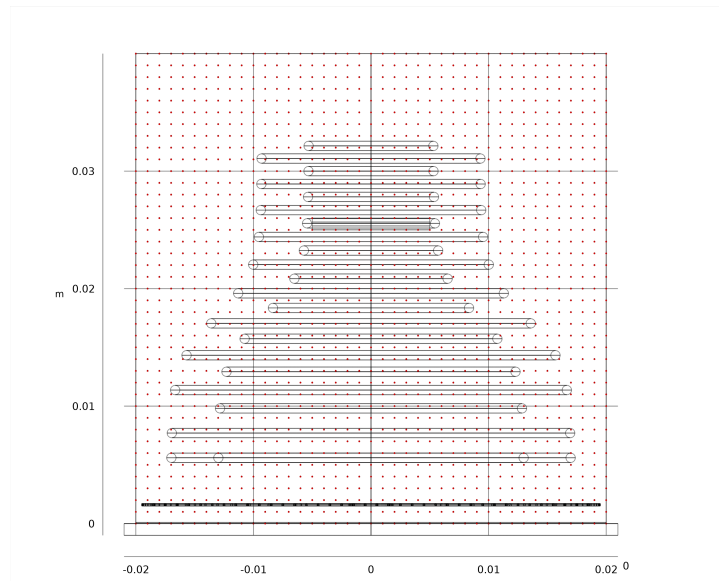


Figure 2.3: Grid points for the field map exported from *COMSOL*. The rendered electric field values were saved to a .txt file and then imported in the *G4beamline* simulation using the *fieldmap* command.

The atomic electron and muonium beams were built and modified using Root packages and imported in the *G4beamline* simulation via the *beam root* command. For the atomic electrons, a uniform distribution in the xz -plane and an initial kinetic energy of 20 eV in random direction was chosen. The muonium beam was modelled following Lambert's cosine law with a waist radius of 50 mm and a momentum of 2.22 keV, corresponding to the kinetic energy of 23.3 meV described in Section [1.2.2](#).

The .root files generated by the *virtualdetector* in the *G4beamline* simulation were analyzed using *Root*. In order to calculate the empirical detection probability, the histogram showing the initial positions of all atomic electrons detected by the *virtualdetector* was divided by the histogram showing the positions of all atomic electrons used as input for the *G4beamline* simulation.

2.2.3 Conductive PLA Tests

In order to test the resistivity of *ProtoPasta*'s commercially available conductive PLA [16] at room temperature, five samples shown in Figure 2.4 were created. They feature black lines of conductive PLA with different lengths and thicknesses attached to substrates made out of normal grey PLA. All samples were designed in *Autodesk Inventor* and 3D-printed using the printer *Ultimaker 3*. The golden connectors were heated up, sunk into the conductive PLA lines and used to connect the voltmeter. All conductive PLA lines had connection ends with dimensions $20 \times 4 \times 4$ mm, as can be seen in Figure 2.4.



Figure 2.4: Samples used to test the resistivity of the conductive PLA at room temperature. They feature black lines of conductive PLA with different thicknesses and lengths, 3D-printed onto ordinary gray PLA. The golden connectors were used to connect the voltmeter.

Chapter 3

Results and Discussion

3.1 Modifications of the ^3He Cryostat

The modifications of the ^3He cryostat decreased the final operating temperature from 0.5 K to 0.42 K. This shows that there is indeed a problem with pre-cooling. Further modifications need to be implemented to bring the final temperature down to the desired 0.3 K.

An issue we are suspecting are cold bridges via the ^4He capillaries. These reach from the bottom of the ^4He cryostat to the target chamber and are pre-cooled by the ^3He system along the way (see Figure 1.4). If superfluid ^4He film fills the capillaries, a thermal connection between the bottom of the ^4He cryostat at roughly 1.3 K and the ^3He system at a temperature below 1 K exists. This could be circumvented by adding a superfluid leak tight valve to the ^4He capillaries.

A further idea would be to move the needle valve from the top of the spiral tube of the ^3He system to its bottom. In that way, the flow of the ^3He liquid would be restricted inside the tube and it would spend more time being cooled by the ^3He vapor. This enhances the pre-cooling further.

Finally, left with no other options, one could change from ^3He evaporation refrigeration to ^3He - ^4He dilution cooling. ^3He - ^4He dilution coolers make use of a quantum effect that causes the phases of ^3He and ^4He not to separate completely at 0 K, as one might expect classically. This phenomenon is again caused by the large effect of the zero-point energy in helium (see 1.3.1 [15]. At 0 K, ^3He has a concentration of 6.6 % in the ^4He phase (hence referred to as the dilute phase), while the ^3He remains pure. By pumping ^3He from the dilute phase, ^3He atoms from the pure phase have to cross the phase boundary, this extracts heat from the system. ^3He - ^4He dilution coolers do not have the $e^{-L/RT}$ -dependence and are hence able to reach temperatures as low as 10 mK. However, while their cooling power does not show the exponential temperature dependence, it is much lower than the one for ^3He evaporation above roughly 0.35 K.

3.2 Acceleration Grid Setup

3.2.1 COMSOL Simulation

Basic Acceleration Grid Setup

The basic setup to accelerate the atomic electrons is given in Figure 3.1. A bell-shaped acceleration grid consisting of ten rings is placed in the cylindrical cavity with a radius of 20 mm and a height of 40 mm. The muonium atoms are ejected from the SFHe layer with a velocity of $\sim 6 \times 10^3 \text{ m s}^{-1}$, hence they travel $\sim 1.3 \text{ cm}$ per lifetime. Due to the bell-shape, most muonium atoms decay within the acceleration grid. The atomic electrons are released isotropically with a kinetic energy of $\sim 20 \text{ eV}$, accelerated towards the top and finally detected by the 10 mm diameter scintillator.

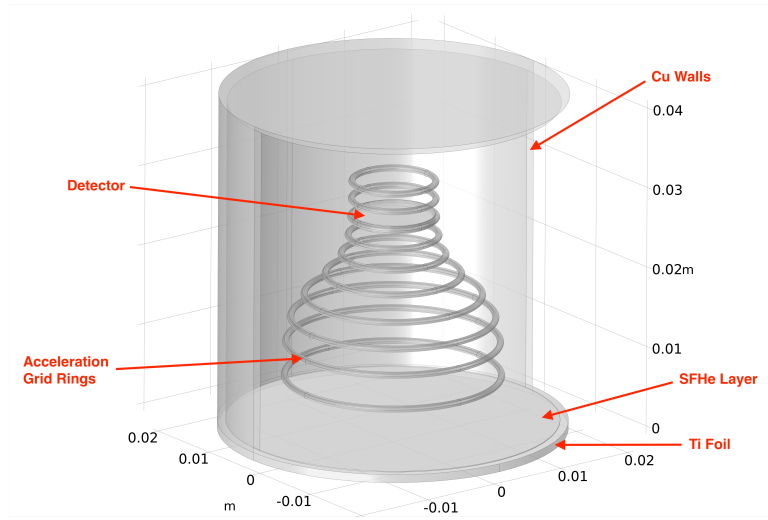


Figure 3.1: Basic acceleration grid setup. The muonium particles are ejected from the SFHe layer at the bottom and decay inside the bell-shaped acceleration grid. The daughter electrons are then accelerated towards the detector at the top.

In order to accelerate the atomic electrons, the grid rings need to be put on positive voltages. The cavity walls are held on ground. The exact values are given by the voltage function displayed in Figure 3.2. Its analytic form is

$$V_{\text{basic}}(z) = \begin{cases} V_{\text{max}} \cdot \left(\frac{z}{1.1 \cdot z_{\text{det}}} \right)^{1.3}, & \text{if } z < 1.1 \cdot z_{\text{det}} \\ V_{\text{max}}, & \text{else} \end{cases} \quad (3.1)$$

where $V_{\text{max}} = 13 \text{ kV}$ is the maximum voltage and $z_{\text{det}} = 25 \text{ mm}$ is the height of the detector. The potential is increased up to $1.1 \cdot z_{\text{det}}$, such that the electric field is still pointing upwards at the height of the detector. It is then held constant to reduce the field at the top. There needs to be a tradeoff between having a low potential gradient at the bottom of the cavity to minimize the field strength inside the SFHe layer and having a potential gradient large enough to accelerate the electrons within reasonable time. The $z^{1.3}$ -dependence was found to achieve this by providing a slightly lower gradient for small z and an increased one for larger z .

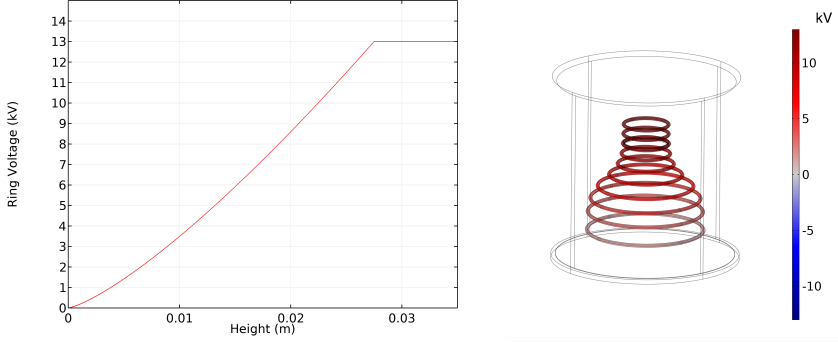


Figure 3.2: Voltage function for the acceleration grid rings. The voltages increase with a $z^{1.3}$ -dependence up to the height of the detector. There they take on a constant value of 13 kV.

The analytic form of the ring radii is

$$R(z) = R_{\max} + (R_{\min} - R_{\min}) \cdot \left(1 - \frac{1}{1 + \exp(-\lambda(z - z_0))}\right), \quad (3.2)$$

where $R_{\max} = 13$ mm, $R_{\min} = 5$ mm, $z_0 = 17.5$ mm and $\lambda = 0.5$ mm $^{-1}$. This results in the bell-shape of the acceleration grid, displayed in Figures 3.1 and 3.2. The parameters λ and z_0 were optimized, finding a compromise between having large $R(z)$ to collect as many electrons as possible, while not having too large gradients $\frac{d}{dz}R(z)$, since otherwise the electron trajectories do not converge radially.

The resulting electric field for the basic acceleration grid setup is displayed in Figure 3.3. The colors show the electric field strength, the arrows point towards the direction of the force exerted on the electrons (negative field direction).

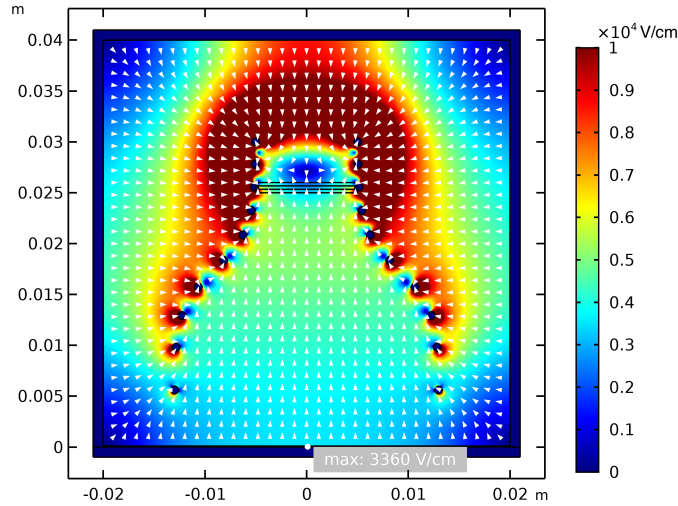


Figure 3.3: Electric field plot for the basic acceleration grid setup. The field inside the grid moves the electrons upwards to the detector. The field outside the grid is pointing inwards, this is not desirable. Background electrons produced by particles hitting the metal cavity walls might be detected as well. In addition, the maximal field strength of 3000 V cm $^{-1}$ inside the SFHe is far above the required 100 V cm $^{-1}$.

While this setup meets the very basic requirements – it collects the atomic electrons and accelerates them towards the detector –, there are several shortcomings. Firstly, the maximal electric field strength inside the SFHe layer amounts to more than 3000 V cm^{-1} , far above the required 100 V cm^{-1} . Secondly, also electrons outside the grid are moved to the center, where they are accelerated towards the detector. Secondary electrons produced by particles hitting the metal walls therefore might also be registered by the detector.

Protection Grid

In order to overcome the first shortcoming of the basic setup – the high electric field strength inside the SFHe layer –, a protection grid consisting of wires on ground voltage could be employed. Such a setup is shown in Figure 3.4. The wires of the protection grid have a diameter of 0.2 mm and a spacing of 0.5 mm. The whole protection grid is placed 1.5 mm above the SFHe layer.

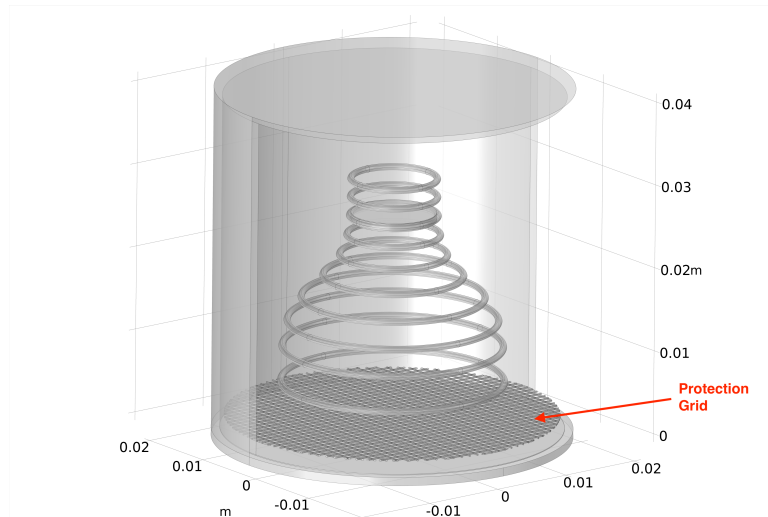


Figure 3.4: Setup with a protection grid above the SFHe layer. The wires of the grid are put on ground voltage, in this way the maximum electric field strength inside the SFHe layer can be reduced.

The resulting field strengths are displayed in Figure 3.5. The maximum field strength of 76 V cm^{-1} inside the SFHe layer now meets the requirements. It could be reduced further at will by making the grid spacing smaller or by moving the protection grid further away from the SFHe layer.

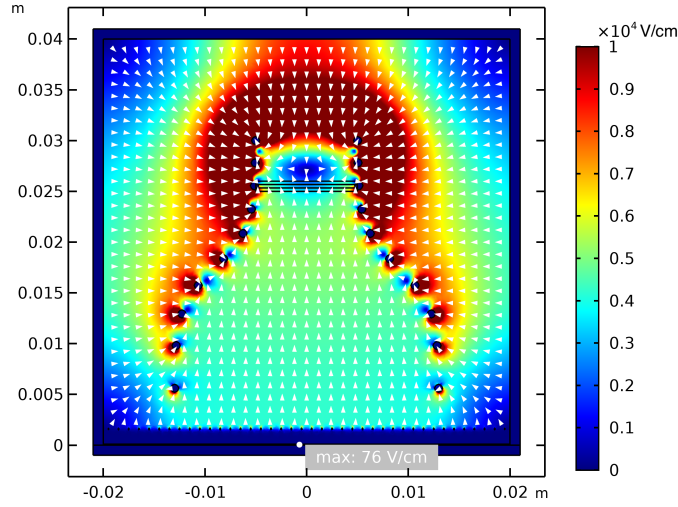


Figure 3.5: Electric field plot for the setup with the protection grid. The maximum field strength below 80 V cm^{-1} inside the SFHe layer now meets the requirements.

Rejection of Secondary Electrons

The mitigation of the second shortcoming – the potential detection of secondary electrons that were freed from the cavity walls – is a bit more involved. Discussing the problem with my supervisors, we came up with four setups that could potentially address this issue. All four are displayed in Figure 3.6. Setup (a) is clearly favorable, as will become clear in the following analysis.

The two setups (a) and (b) on the top row feature two cages. For the inner cage, the voltage function $V(z) = V_{\text{basic}}(z)$ of the basic setup was reused (see Equation 3.1). In that way the atomic electrons are accelerated towards the top. The outer protection cage circumvents the detection of secondary electrons. In setup (a), the protection cage is put on negative voltages $V(z) = -V_{\text{basic}}(z)$, repelling the secondary electrons. Setup (b) features a protection cage with high positive voltages $V(z) = 1.5 \cdot V_{\text{basic}}(z)$, collecting the secondary electrons.

Setups (c) and (d) feature only one cage with negative voltages $V(z) = V_{\text{basic}}(z) - V_{\text{max}}$. In (c), the foil below the SFHe is biased negatively with $V = -V_{\text{max}}$, the same is true for the protection grid above the SFHe. In that way, atomic atoms released by decaying muonium atoms above the protection grid are accelerated towards the top of the cage. At the same time, secondary electrons are rejected. In setup (d), two protection grids are used. The lower one is put on ground to protect the SFHe layer against high field strengths. The upper grid is put on a negative voltage $V = -V_{\text{max}}$ to accelerate the atomic electrons towards the top.

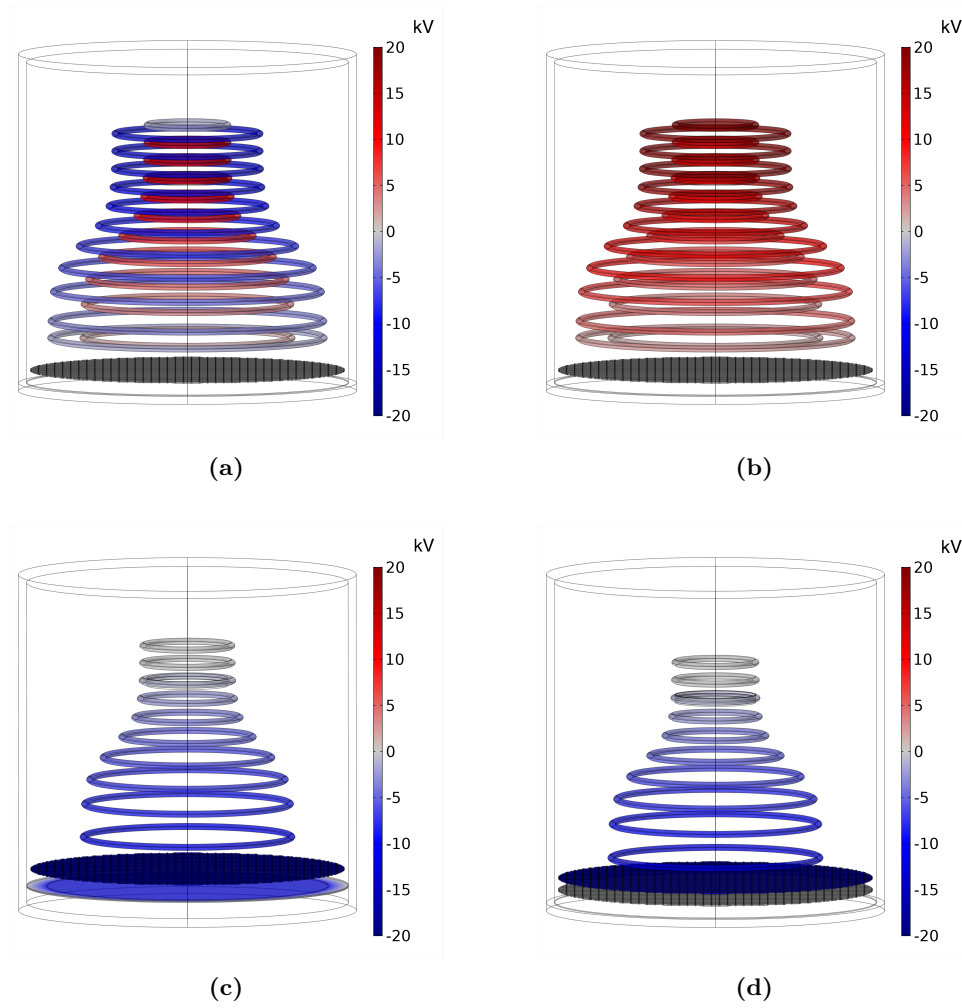


Figure 3.6: Setups for the rejection of secondary electrons. The setups on the upper row involve two grids, a positively charged inner one for the acceleration of the electrons inside the bell-shaped geometry and an outer one to reject or collect secondary electrons. The setups on the lower row feature an acceleration grid with negative voltages and either a negatively biased foil or a second protection grid added on top of the first one.

The resulting electric field strengths are shown in Figure 3.7.

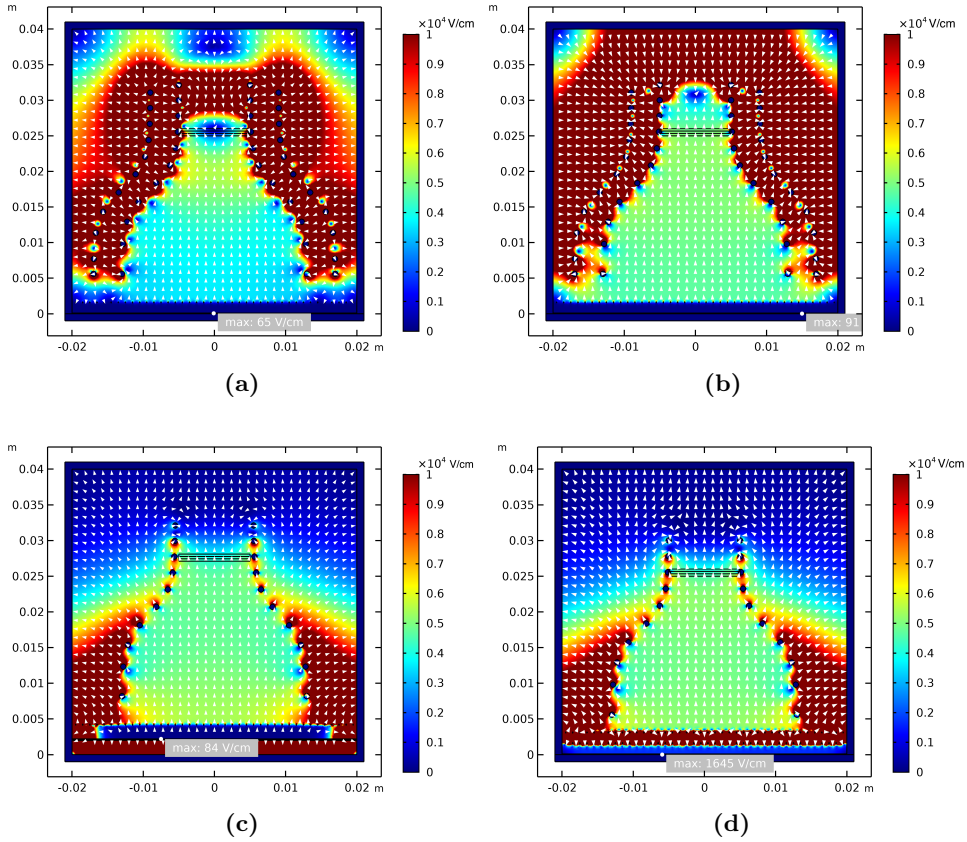


Figure 3.7: Electric field strengths for the four setups. The white arrows indicate the direction of the forces on the electrons (negative field direction). While the field distribution of setup (a) satisfies all requirements, the fields in (b) and (c) do not collect the atomic electrons and the field strengths in (d) are far too high inside the SFHe layer.

Setup (a) features a low field strength in the SFHe layer, a force field that is uniformly pointing upwards inside the bell-shaped acceleration grid as well as reduced field strengths at the position of the detector and at the top of the cavity. The latter was achieved by reducing the voltage of the uppermost cage ring (see Figure 3.6a). The force field between the cages is pointing inwards, this is crucial for the collection of atomic electrons.

While setups (b) and (c) meet the requirement of having field strengths below 100 V cm^{-1} inside the SFHe layer, they have a major inadequacy: the force field at the edge of the inner bell-shaped geometry is pointing outwards. Therefore, the atomic electrons are not collected, all electrons not released vertically below the detector are lost. This will be shown explicitly in the *G4beamline* simulations discussed in Section 3.2.2.

Setup (d) can be rejected on the basis that the maximum field strength of more than 1600 V cm^{-1} is significantly above limit.

3.2.2 G4beamline Simulation

Electron Trajectories

The trajectories of the atomic electrons in the field configurations of setups (a)-(c) were modelled in *G4beamline* simulations. Setup (d) was not pursued further, as the field strengths inside the SFHe layer exceed 100 V cm^{-1} . In the simulation, the atomic electrons were distributed randomly in the xz-plane and given an initial energy of 20 eV. Figure 3.8 shows the resulting electron trajectories.

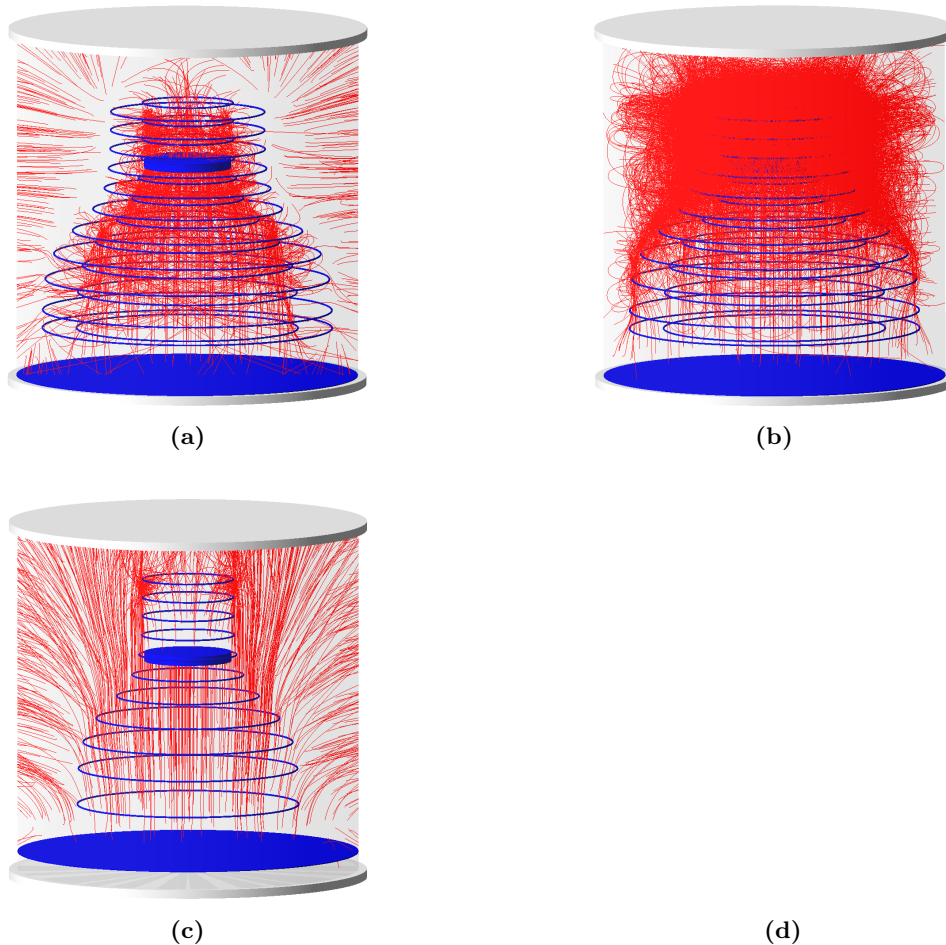


Figure 3.8: Trajectories of 1'000 atomic electrons released at random positions for the four setups. As expected, the primary atomic electrons in setup (a) converge towards the detector, while secondary electrons released outside the cage are rejected. For setups (b) and (c), the trajectories of the atomic electrons do not converge. Setup (d) was not pursued further, as it features field strengths above 100 V cm^{-1} inside the SFHe layer.

In setup (a), all trajectories of electrons released within the bell-shaped geometry end up at the detector. Electrons released outside the cage are rejected. In setups (b) and (c), the trajectories of the electrons that should be collected do not converge. Worse than that, in setup (b) many of the electrons outside the cage are accelerated inwards, where they spiral around the detector. This results in the mess of trajectories shown above.

Above results show that setup (a) is favorable. The detailed detection probabilities for atomic electrons released at different positions inside the cavity using setup (a) are given in Figure 3.9. The probabilities are generally high inside the bell-shaped geometry, while being low or even vanishing outside the two cages.

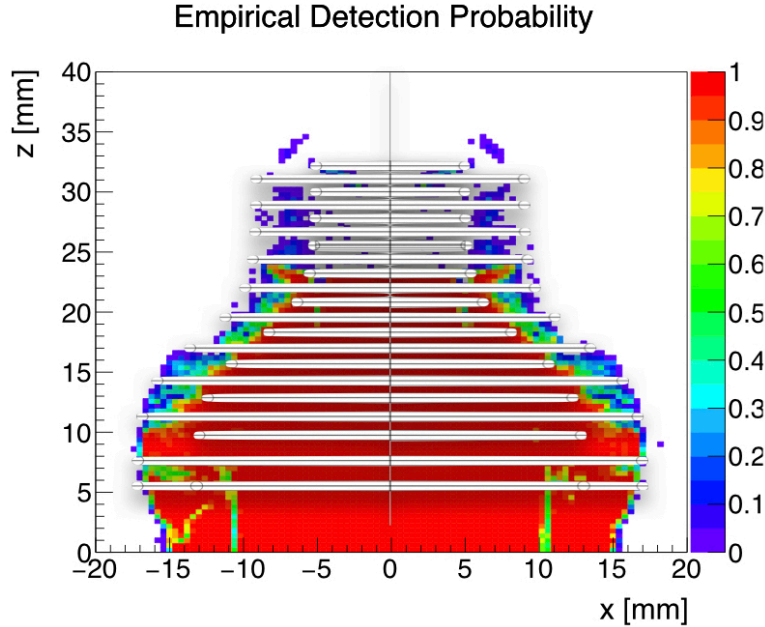


Figure 3.9: Detection probabilities for atomic electrons released at different positions in the cavity using setup (a). Generally, the probabilities inside the bell-shaped acceleration grid are high, while the probabilities outside the two grids are vanishing.

Muonium Beam

In order to calculate the overall detection probability of electrons released in muonium decays, the muonium beam was modelled in *G4beamline* following Lambert’s cosine law. Here, the cosine law can be viewed as the most pessimistic scenario, as it describes particles being ejected diffusely from a surface [20, p. 13]. The beam was assumed to have a waist radius of 50 mm and a momentum of 2.22 keV/c, corresponding to the kinetic energy of 23.3 meV. The trajectories for 1’000 events are given on the left in Figure 3.10, a histogram showing the resulting decay positions for 1’000’000 events is given on the right.

As expected, most of the Muonium atoms decay within a few centimeters after being ejected from the SFHe layer. By multiplying the decay positions in Figure 3.10 by the detection probabilities for atomic electrons at the respective positions in Figure 3.9, the overall detection probability for atomic electrons resulting from muonium decays can be determined. It amounts to 85.2%. This proves that setup (a) is efficient in collecting the atomic electrons released in muonium decays.

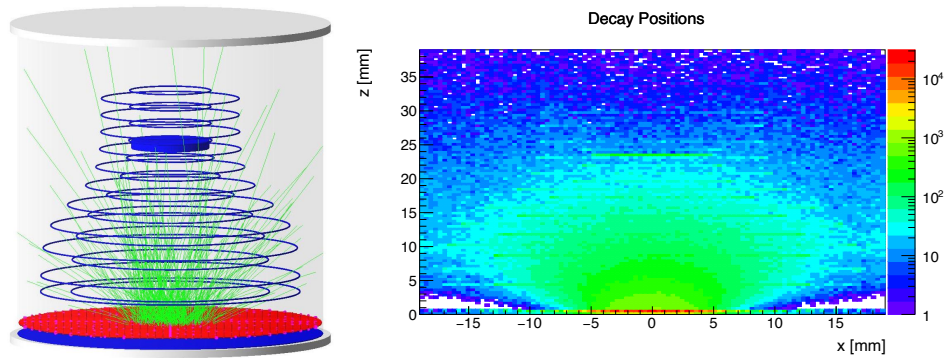


Figure 3.10: Muonium beam modelled in G4BL. The angular dependence of the beam force follows Lambert's cosine law. The trajectories for 1'000 events are displayed on the left. The histogram on the right shows the decay positions of the Muonium atoms (the colors indicate the number of particles that decayed in that region).

3.2.3 Conductive PLA Tests

The results of the conductive PLA tests at room temperature are given in Figures [3.11](#) and [3.12](#). The resistance of the PLA was found to be explained well by a linear model, the R^2 value of the fit being 0.91. The specific resistivity is $9.2(5) \Omega \text{ mm}^{-1}$.

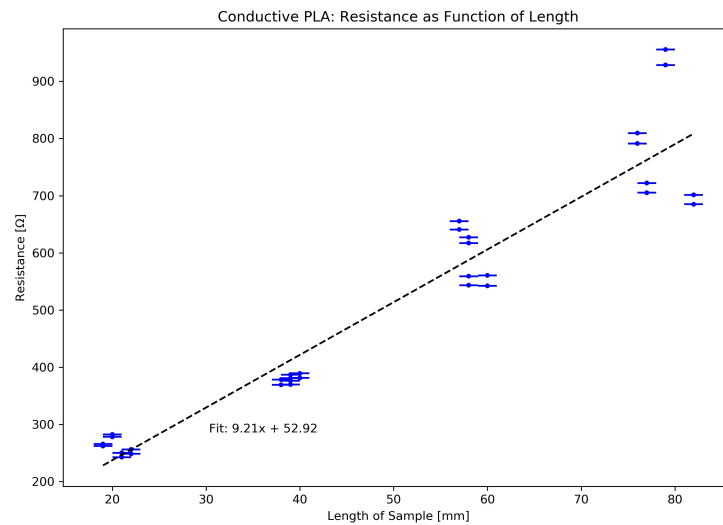


Figure 3.11: Resistivity as a function of length for the conductive PLA at room temperature. The linear model explains the data well, the R^2 value is 0.91.

Also the resistance as a function of inverse area seems to follow a linear trend, the R^2 value of the fit being 0.99. Here, the specific resistivity is $8600(100) \Omega \text{ mm}^2$.

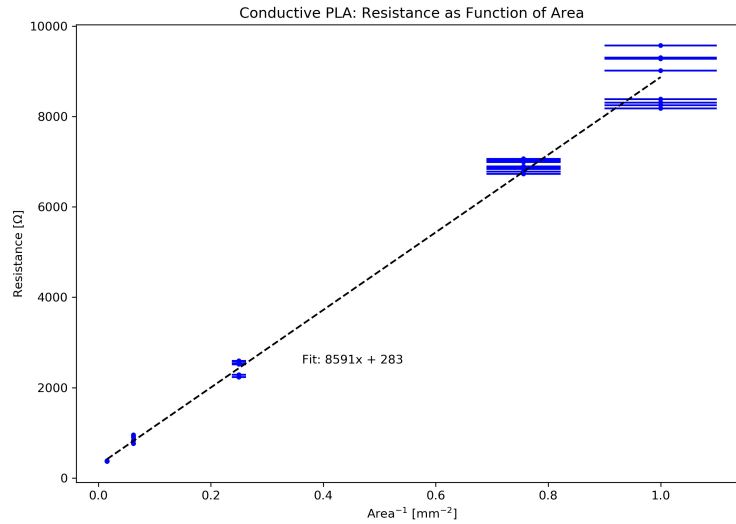


Figure 3.12: Resistivity as a function of area for the conductive PLA at room temperature. The linear model explains the data well, the R^2 value is 0.99.

In order to test the temperature dependence of the conductive PLA at low temperatures, cryogenic tests need to be carried out. These will show whether the general temperature trend shown in Figure [L.7](#) for carbon black networks also holds for ProtoPasta Inc.'s PLA. Due to the Covid-19 outbreak and the resulting shutdown of PSI, these tests had to be postponed.

Chapter 4

Conclusion

In order to reach the ambitious goal of measuring the gravitational acceleration of second generation antimatter, upfront research and development is required for all stages of the muonium antimatter gravity experiment. A novel method to produce a high quality cold muonium beam is needed to achieve the required interferometer stability, the interferometer needs to be aligned to nanometer precision and the electrons and positron resulting from the muonium decays need to be detected reliably without interfering with the previous stages.

Concerning stage (1) of the experiment, the operating temperature of the ^3He evaporation cryostat was decreased from 0.5 K to 0.42 K by enhancing the pre-cooling. Further modifications proposed in Section 3.1 will be implemented in the near future, this will hopefully reduce the operating temperature of the cryostat to the required 0.3 K. Also the implementation of a ^3He - ^4He dilution cooler is being considered. The presented considerations might be instructive for other cryogenic setups where evaporation cooling is employed.

As for stage (3) of the experiment, the design and fabrication of the acceleration grid for the atomic electrons resulting from muonium decays were discussed. Constraints placed on the acceleration grid, such as having a field strength below 100 V cm^{-1} at the bottom and rejecting secondary electrons freed from the cavity walls, required careful modeling of the setup. In this thesis, a setup meeting all constraints was presented. It features two cages: an inner acceleration cage and an outer protection cage to repel secondary electrons, as well as a protection grid at the bottom to shield the SFHe layer from high field strengths. While future modifications of the experimental setup might require amendments to the exact geometry of the acceleration cage, the geometry presented here can be viewed as a proof of concept meeting all requirements.

Finally, the possibility of fabricating the grid wires using 3D printing with conductive PLA was assessed. The tests at room temperature were promising, indicating that conductive PLA is likely to be increasingly used in future setups where a precise conductive geometry is required. The specific resistivities per length and area we measured at room temperature were $9.21 \Omega \text{ mm}^{-1}$ and $8591 \Omega \text{ mm}^2$, respectively. Measurements of the exact temperature dependence of the PLA conductivity at cryogenic temperatures had to be postponed due to the Covid-19 outbreak.

In gloomy times like these, we need brave scientific endeavors more than ever. I like to think that performing the first measurement of the gravitational acceleration of an antiparticle ever, period, as well as the first measurement of the gravitational acceleration of a second generation particle ever, period, falls in that category.

Acknowledgements

First and foremost, I would like to wholeheartedly thank Dr. Anna Soter for all the help, advice, practical tricks, interesting discussions, tea and tea cups, Ghostbusters pictures and much more. You were a wonderful supervisor! Warm thanks also go to PHD candidate Jonas Nuber for helping me with the *G4 Beamline* simulations and sharing his *Root* scripts with me, for explaining the details of experimental setups standing around and for his unbroken support that made G4Beamline-build-with-adsorption-final-final-2 possible. Furthermore, big thanks go to Dr. Aldo Antognini for all the discussions, advice and explanations about fascinating low energy particle physics topics both during the Semester thesis and in his lecture. I would also like to thank PHD candidate Patrick Schwendimann for all the tea, PHD candidate Nicholas John Ayres for the delicious Christmas cake and PHD candidate Manuel Zeyen for the interesting tour of the muonic hydrogen spectroscopy laser system. My gratitude also goes to Dr. Andreas Knecht, Dr. Frank Meier Aeschbacher, Dr. Karsten Reinhard Schuhmann, PHD candidate Narongrit Ritjoho and all the other people of PSI's Muon Physics group for all the wonderful discussions. Last but certainly not least, I would like to thank Prof. Dr. Klaus Kirch for all his support, advice and for letting me carry out this Semester thesis in his research group.

Bibliography

- [1] J. Erler and M. Schott, “Electroweak precision tests of the Standard Model after the discovery of the Higgs boson,” *Progress in Particle and Nuclear Physics*, vol. 106, p. 68–119, May 2019.
- [2] D. Hanneke, S. Fogwell, and G. Gabrielse, “New measurement of the electron magnetic moment and the fine structure constant,” *Phys. Rev. Lett.*, vol. 100, p. 120801, Mar 2008.
- [3] R. S. Park, W. M. Folkner, A. S. Konopliv, J. G. Williams, D. E. Smith, and M. T. Zuber, “Precession of Mercury’s Perihelion from Ranging to the MESSENGER Spacecraft,” *The Astronomical Journal*, vol. 153, no. 3, p. 121, feb 2017.
- [4] R. Ellis, “Gravitational lensing: A unique probe of dark matter and dark energy,” *Philosophical transactions. Series A, Mathematical, physical, and engineering sciences*, vol. 368, pp. 967–87, 03 2010.
- [5] LIGO Scientific Collaboration and Virgo Collaboration, “Observation of Gravitational Waves from a Binary Black Hole Merger,” *Phys. Rev. Lett.*, vol. 116, p. 061102, Feb 2016.
- [6] P. Touboul, G. Métris, M. Rodrigues, Y. André, Q. Baghi, J. Bergé, D. Boulanger, S. Bremer, R. Chhun, B. Christophe, and et al., “Space test of the equivalence principle: first results of the MICROSCOPE mission,” *Classical and Quantum Gravity*, vol. 36, no. 22, p. 225006, Oct 2019.
- [7] A. Zhmoginov, C. Amole, M. Ashkezari, M. Baquero-Ruiz, W. Bertsche, E. Butler, A. Capra, C. Cesar, M. Charlton, S. Eriksson, J. Fajans, T. Friesen, M. Fujiwara, D. Gill, A. Gutierrez, J. Hangst, W. Hardy, M. Hayden, C. Abiodun, and A. Charman, “Description and first application of a new technique to measure the gravitational mass of antihydrogen,” *Nature Communications*, vol. 4, p. 1785, 04 2013.
- [8] A. Antognini, D. Kaplan, K. Kirch, A. Knecht, D. Mancini, J. Phillips, T. Phillips, R. Reasenberg, T. Roberts, and A. Soter, “Studying Antimatter Gravity with Muonium,” *Atoms*, vol. 6, no. 2, p. 17, Apr 2018.
- [9] D. S. M. Alves, M. Jankowiak, and P. Saraswat, “Experimental constraints on the free fall acceleration of antimatter,” 2009.
- [10] ALPHA Collaboration, “Description and first application of a new technique to measure the gravitational mass of antihydrogen,” *Nature Communications*, vol. 4, no. 1, p. 1785, 2013.
- [11] AEGIS Collaboration, “Probing antimatter gravity - the AEGIS experiment at CERN,” *EPJ Web Conf.*, vol. 126, p. 02016, 2016.

-
- [12] P. Perez and Y. Sacquin, “The GBAR experiment: gravitational behaviour of antihydrogen at rest,” *Classical and Quantum Gravity*, vol. 29, no. 18, p. 184008, aug 2012.
- [13] D. B. Cassidy and S. D. Hogan, “Atom control and gravity measurements using Rydberg positronium,” in *International Journal of Modern Physics Conference Series*, ser. International Journal of Modern Physics Conference Series, vol. 30, May 2014, p. 1460259.
- [14] D. Taqqu, “Ultraslow Muonium for a Muon beam of ultra high quality,” *Physics Procedia*, vol. 17, pp. 216 – 223, 2011, 2nd International Workshop on the Physics of fundamental Symmetries and Interactions - PSI2010.
- [15] F. Pobell, “Matter and methods at low temperatures,” *Matter and Methods at Low Temperatures*, pp. 1–461, 01 2007.
- [16] “Conductive PLA - ProtoPasta,” <https://www.proto-pasta.com/pages/conductive-pla>, accessed: 2019-02-04.
- [17] R. Rothon, *Fillers for polymer applications*. Springer, 2017.
- [18] A. Király and F. Ronkay, “Temperature dependence of electrical properties in conductive polymer composites,” *Polymer Testing*, vol. 43, pp. 154 – 162, 2015.
- [19] “COMSOL Multiphysics Modeling Software,” <https://www.comsol.com>, accessed: 2019-12-18.
- [20] F. L. Pedrotti and L. S. Pedrotti, *Introduction to optics*. Prentice-Hall, Inc., 1993.

Declaration of Originality

I hereby declare that the written work I have submitted entitled

Acceleration Cage for Atomic Electron Detection in Muonium Antimatter Gravity Experiment

is original work which I alone have authored and which is written in my own words.¹

Author(s)

Luc Schnell

Supervising lecturer

Anna Soter

With the signature I declare that I have been informed regarding normal academic citation rules and that I have read and understood the information on 'Citation etiquette' (<https://www.ethz.ch/content/dam/ethz/main/education/rechtliches-abschluesse/leistungskontrollen/plagiarism-citationetiquette.pdf>). The citation conventions usual to the discipline in question here have been respected.

The above written work may be tested electronically for plagiarism.

Bern, 8.6.2020

Place and date



Signature

¹Co-authored work: The signatures of all authors are required. Each signature attests to the originality of the entire piece of written work in its final form.